

Article

Geochemistry of Magmatic and Xenocrystic Spinel in the No.30 Kimberlite Pipe (Liaoning Province, North China Craton): Constraints on Diamond Potential

Ren-Zhi Zhu ^{1,2}, Pei Ni ^{1,*}, Jun-Ying Ding ¹ and Guo-Guang Wang ¹

¹ State Key Laboratory for Mineral Deposit Research, Institute of Geo-Fluids, School of Earth Science and Engineering, Nanjing University, Nanjing 210023, China; rzzhu@smail.nju.edu.cn or r.zhu@campus.unimib.it (R.-Z.Z.); jyding@nju.edu.cn (J.-Y.D.); ggwang@nju.edu.cn (G.-G.W.)

² Department of Earth and Environmental Sciences, University of Milano-Bicocca, Milan 20126, Italy

* Correspondence: peini@nju.edu.cn

Received: 29 April 2019; Accepted: 23 June 2019; Published: 24 June 2019



Abstract: There are two genetic types of spinel (magmatic spinel crystallizing directly from kimberlite magma and xenocrystic spinel derived from mantle xenoliths) in the No.30 kimberlite pipe (Liaoning Province, North China Craton). Their geochemistry is investigated to reveal processes of diamond capture and resorption during kimberlite magmatism to constrain the diamond potential. Magmatic spinels are mostly euhedral to subhedral, 20 to 60 μm in size, and have compositional zones: the cores are classified as chromite with high Cr and Mg contents, and the rims are classified as magnetite with low Cr and high ferric Fe. The compositional trends suggest that magmatic spinel and olivine phenocrysts are crystallized contemporaneously during the early stages of kimberlite crystallization. During this period, temperature (T) and oxygen fugacity (fO_2) values calculated at an assumed pressure of 1 GPa are in the range of 994–1274 $^{\circ}\text{C}$ and 1.6–2.4 $\log fO_2$ units below the nickel-nickel oxide (NNO) buffer, respectively. The high values of fO_2 suggest heavy diamond resorption during kimberlite magmatism. Estimated temperatures of xenocrystic spinel range from 828 to 1394 $^{\circ}\text{C}$, and their distributions indicate that only a small proportion of xenocrystic spinels are derived from the diamond stabilization field, which suggests a low potential of diamond capture. The low diamond capture and heavy diamond resorption during kimberlite magmatism contributed to the low diamond grade of the No.30 kimberlite.

Keywords: geochemistry; magmatic spinel; xenocrystic spinel; kimberlite; diamond potential

1. Introduction

Diamond exploration relies on mantle-derived “indicator minerals” because they commonly occur as inclusions within diamonds, and thus, play an important role in diamond formation. The widely utilized indicator minerals include garnet, chromite, clinopyroxene, and ilmenite [1–13]. The use of chromite in diamond exploration has concentrated on the recognition of grains similar in the major-element composition to chromite inclusions within diamonds [14]. Combined major and trace element compositions for chromite are used to distinguish the source rock of chromite and to discriminate mantle-derived xenocrysts from magmatic spinels [4]. In addition, the Zn-in-chromite thermometer (proposed by Ryan et al. [15] based on the strong temperature-dependence of the partitioning of Zn between chromite and olivine) further divides chromite xenocrysts from kimberlite into those derived from the diamond stability field and those from shallower, barren levels of

mantle [4,5]. Single-grain temperature estimates are projected onto known geotherm to obtain a depth of origin for each grain [16].

At present, the discrimination of mantle-derived materials (xenoliths and xenocrysts) entrained by kimberlite is the main tool to predict the grade and quality of diamonds transported by the kimberlite to the Earth's surface. However, in recent years, more and more studies focusing on various morphological forms and surface features in natural diamond recovered from kimberlites, show that diamond resorption (dissolution) widely occur during kimberlite magma ascent, which greatly influences the grade and value of diamonds [17,18]. The diamond resorption is greatly controlled by the oxygen fugacity (fO_2) of the kimberlite magma [17,19–21]. A good understanding of the magmatic history of the kimberlite is necessary to ascertain whether diamonds could survive the rapid journey from the upper mantle to the surface of the Earth. It has been shown that spinel commonly forms throughout the kimberlite crystallization [22], and thus the morphology and composition of magmatic spinel may be useful in deciphering the kimberlite crystallization history [23,24], and the temperature and oxygen fugacity in kimberlite magma during magmatic spinel formation could be estimated [25].

In a previous study on xenocrystic spinels from the No.30 kimberlite (Liaoning Province, North China Craton), the authors suggested that the cores of the spinel (classified as magnesiochromite) were remnants of primary mantle xenocrysts, and the intermediate zones (classified as chromite) and the rims (classified as magnetite) formed during kimberlite magmatism [26]. In this study, we report the trace element concentrations of xenocrystic spinels and discuss the differences between magnesiochromites derived from the diamond stability field and those from the barren levels of the mantle [4]. The major element compositions of magmatic spinels are presented and compared with those of the rims in xenocrystic magnesiochromites. The temperature and oxygen fugacity of the No.30 kimberlite magma are estimated in order to discuss the diamond resorption. The diamond potential of the No.30 kimberlite is discussed on the basis of the trace elements signature and temperature estimates of the xenocrystic garnet xenocrysts [27] and spinel (this paper).

2. Samples and Methods

The samples in this study consist of 14 magmatic spinels and 51 xenocrystic spinels from the No.30 kimberlite pipe. The magmatic spinels were prepared as double-polished thin sections and their major compositions were analyzed in this study. Xenocrystic spinels were single crystals obtained by heavy mineral concentration and separation, and their morphology and major elements have been reported in a previous study by Zhu et al. [26]. In this study, we proceeded to analyze their trace element concentrations.

The major elements of magmatic spinel were analyzed at the State Key Laboratory for Mineral Deposit Research, Nanjing University, China, using a JAX 8100 Electron Probe Micro Analyzer (EPMA). The EPMA work was conducted by wavelength dispersive spectrometry (WDS). The analytical conditions were as follows: beam accelerating voltage 20 kV, beam current 20 nA, beam diameter 1 μm , and a counting time of 30 s. A number of natural, as well as synthetic standards, were used for calibration. For the operating conditions, the detection limit for major elements was 0.01 wt. %, and the accuracy was better than 1%. The proportion of Fe^{2+} and Fe^{3+} in the chrome spinel was calculated using stoichiometric and charge balance equations [28].

Trace elements in xenocrystic spinel were investigated at the State Key Lab of Ore Deposit Geochemistry, Institute of Geochemistry, Chinese Academy of Sciences, using a Coherent GeoLasPro 193-nm Laser Ablation system coupled with an Agilent 7700 \times ICP-MS. For spot analysis, a 40 μm spot size was applied with an energy density of ~ 100 mJ per pulse and a repetition rate of 6 Hz. Each analysis contained 20 s for measuring the gas blank and 40 s for data acquisition. Different silicate glass reference materials, including BHVO-2G, BIR-1G, GSE-1G, and NIST610 were used as external standards and ^{57}Fe as an internal standard to calibrate element contents. Quality control of time-dependent drift of sensitivity and mass discrimination was monitored by GSE-1G repeated after every eight analyses. The off-line data processing was performed using the ICPMSDataCal

program [29]. Values were cross-checked against standards BCR-2G. Analytical precision of $\leq 6\%$ was indicated for most elements (Table S1 in Supplementary Materials).

3. Results

3.1. Morphology of Spinel

The No.30 kimberlite was heavily hydrothermally altered. However, the xenocrystic and magmatic spinels were very resistant to alteration and survived as primary minerals. The morphology of xenocrystic spinel has been described by Zhu et al. [26] and will not be repeated here. The magmatic spinels are pervasive in kimberlite, usually euhedral to subhedral, 20 to 60 μm in diameter, and strongly zoned from the chromite core to the magnetite rim (Figure 1A, Table 1). The chromite cores in some magmatic spinels are further divided into Ti-Al-Mg chromite core and Ti-Al chromite intermediate zone (Figure 1B, Table 1). Some spinels show small holes (Figure 1C) that may represent an incipient “lagoon” in an atoll-texture [23], which is the characteristic feature of magmatic spinel in Group I kimberlite [22,30].

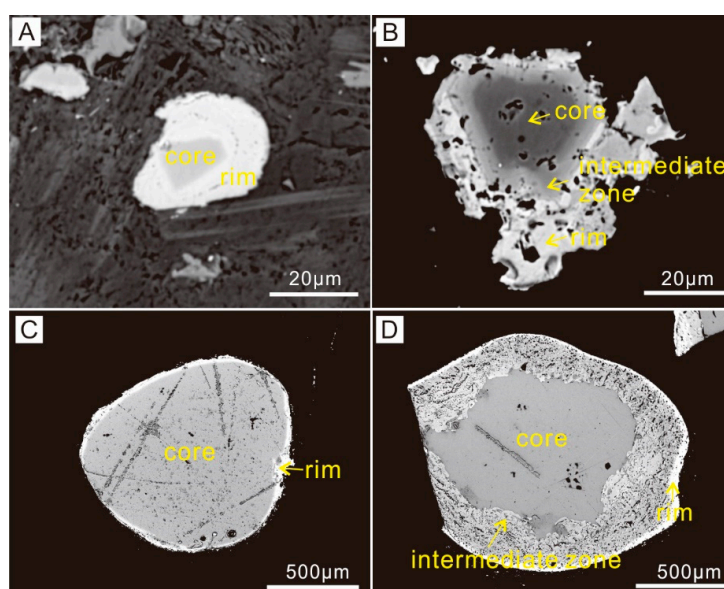


Figure 1. Backscatter electron (BSE) images of magmatic spinels (A,B) and xenocrystic spinels (C,D) from the No.30 kimberlite. Magmatic spinels show compositional zones from the Ti-Al-Mg chromite core through the Ti-Al chromite intermediate to the magnetite rim, and spinel xenocrysts show compositional zones from xenocrystic magnesiochromite core through the Ti-Al-Mg chromite intermediate to the magnetite rim.

3.2. Chemical Composition of Spinel

Magmatic spinels and xenocrystic spinels show compositional zones (Figures 1 and 2). From the cores through the intermediate zones to the rims in the magmatic spinels, there is a continuous decrease in Cr_2O_3 (from 49.8–53.4 through 16.4–46.0 to 0.2–2.7 wt. %) and MgO contents (from 8.1–13.9 through 0.3–4.6 to 0.1–0.7 wt. %); the Al_2O_3 concentrations increase from the cores (4.6–6.5 wt. %) to the intermediate zones (4.5–8.5 wt. %) and decrease sharply in the rims (0.01–1.5 wt. %); the TiO_2 concentrations increase from the cores (3.5–4.6 wt. %) to the intermediate zones (5.2–10.3 wt. %) and decrease sharply in the rims (0.2–4.6 wt. %) (Figure 2, Table 1); and there is a continuous increase in Fe_2O_3 contents (from 7.2–9.7 through 10.2–13.1 to 57.8–65.9 wt. %). The cores of the xenocrystic spinels are discriminated by higher Cr_2O_3 and MgO and lower TiO_2 and Fe_2O_3 compared with magmatic spinels (Figure 2), which supports the xenocrystic origin [26]. The intermediate zones and rims of xenocrystic spinels are suggested to form in the host kimberlite magma and can be linked to the magmatic spinels [26]. As shown in Figure 2, the rims of xenocrystic spinels show

low Cr_2O_3 , MgO , Al_2O_3 , and high Fe_2O_3 contents, which can be linked to the rims in the magmatic spinels. The intermediate zones of xenocrystic spinels show a wider range in Al_2O_3 and Cr_2O_3 concentrations, which shows more affinity to the cores of the xenocrystic spinels rather than the cores of the magmatic spinels; however, their MgO , TiO_2 , and Fe_2O_3 concentrations are consistent with the latter. Moreover, in the spinel prisms ([23] and references therein), the cores of the magmatic spinel and intermediate zones of xenocrystic spinels are classified as chromite, the rims of the magmatic spinels and xenocrystic spinels are classified as magnetite, and the cores of the xenocrystic spinels are classified as xenocrysts (Figure 3).

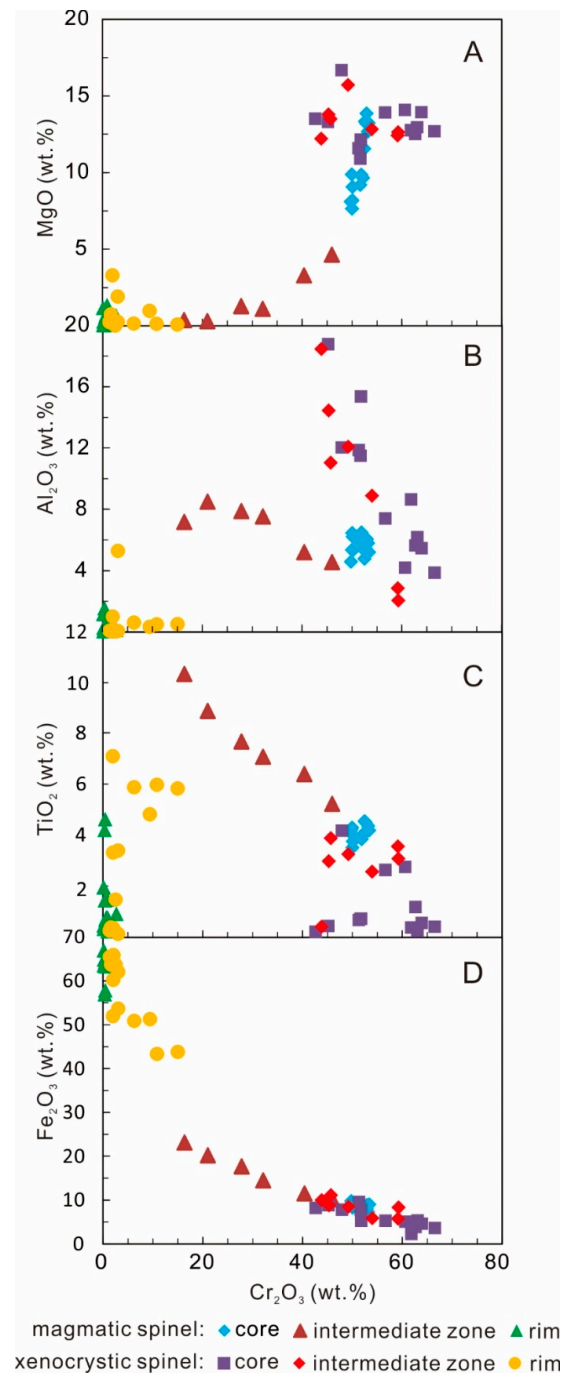


Figure 2. Variations of MgO (A), Al_2O_3 (B), TiO_2 (C), and Fe_2O_3 (D) versus Cr_2O_3 contents in the magmatic and xenocrystic spinels from the No.30 kimberlite.

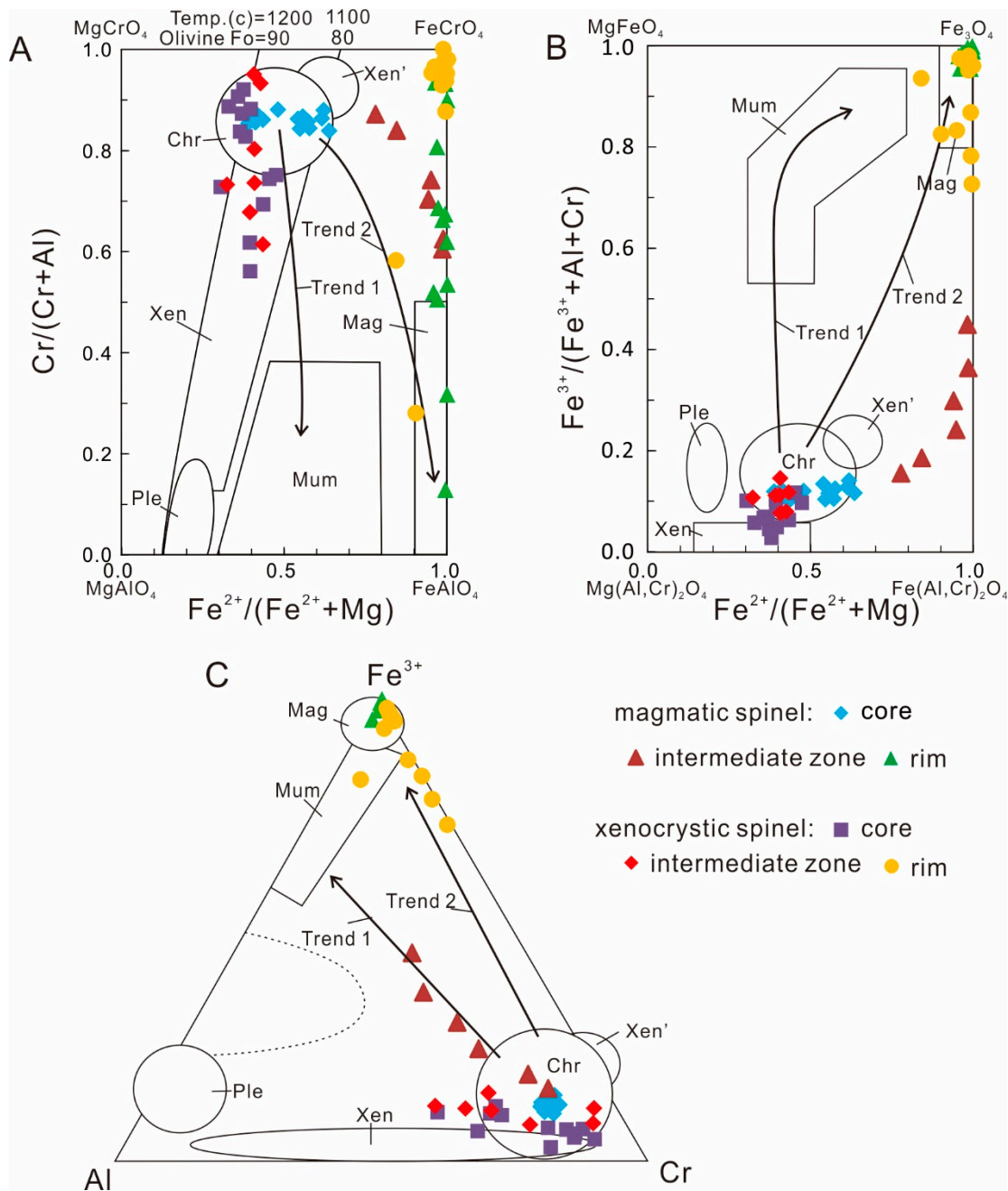


Figure 3. Three spinel projections of oxidized spinel prism for magmatic and xenocrystic spinels from the No.30 kimberlite pipe: **(A)** Cr/(Cr + Al) versus Fe²⁺/(Fe²⁺ + Mg), **(B)** Fe³⁺/(Fe³⁺ + Al + Cr) versus Fe²⁺/(Fe²⁺ + Mg) and **(C)** Fe³⁺-Al-Cr. The iso-potential lines (dotted lines) indicating that the composition of the spinels that is in equilibrium with olivine (Fo 90 and 80) at a constant temperature of 1200 °C and 1100 °C is after Irvine (1965). Curves of trend 1 and trend 2 are after Mitchell [22] and Roeder and Schulze [23]. Abbreviations: Xen = xenocryst peridotite spinel; MUM = magnesium-ulvöspinel-magnetite; Chr = chromite; Xen' = Metasomatized xenocryst peridotite spinel; Mag = magnetite.

Table 1. Mineral chemistry (oxide wt. %) of magmatic spinels from the No.30 kimberlite.

Oxide (wt. %)	WFD148-SP1			WFD148-SP2			WFD148-SP3			WFD148-SP4			WFD148-SP5			WFD148-SP6			WFD148-SP7		
	Core	Rim	Core	Rim	Core	Rim	Core	Rim	Core	Rim	Core	Rim	Core	Rim	Core	Rim	Core	Rim	Core	Rim	
TiO ₂	3.84	0.35	3.92	0.79	3.99	0.69	3.51	0.34	4.20	0.39	3.75	0.24	4.04	0.77							
Al ₂ O ₃	6.49	0.03	5.76	0.22	5.30	0.34	6.45	0.08	4.58	0.43	6.21	0.05	5.38	0.15							
Cr ₂ O ₃	51.86	1.57	51.67	0.72	50.11	0.53	50.04	0.23	49.75	0.70	50.13	0.97	52.22	0.95							
Fe ₂ O ₃	7.47	65.87	7.38	63.38	8.92	63.36	8.23	64.88	9.71	63.48	8.90	64.81	8.24	64.27							
FeO	21.21	30.72	21.92	29.34	23.21	29.14	23.80	29.39	23.48	28.46	22.02	29.68	21.57	29.72							
MgO	9.85	0.17	9.18	0.51	8.18	0.56	7.63	0.28	8.09	0.74	9.07	0.14	9.64	0.57							
MnO	0.58	0.01	0.56	0.18	0.81	0.09	0.80	0.08	0.75	0.12	0.63	0.16	0.69	0.12							
Total	101.30	98.71	100.38	95.14	100.53	94.71	100.46	95.27	100.56	94.32	100.69	96.04	101.77	96.55							
Ti	0.096	0.010	0.100	0.024	0.102	0.021	0.090	0.010	0.108	0.012	0.095	0.007	0.101	0.023							
Al	0.255	0.002	0.230	0.011	0.213	0.016	0.259	0.004	0.185	0.021	0.247	0.002	0.212	0.007							
Cr	1.366	0.048	1.383	0.023	1.353	0.017	1.349	0.007	1.348	0.022	1.337	0.031	1.378	0.030							
Fe ³⁺	0.187	1.930	0.188	1.919	0.229	1.925	0.211	1.969	0.250	1.933	0.226	1.953	0.207	1.917							
Fe ²⁺	0.591	1.000	0.620	0.987	0.663	0.984	0.679	0.991	0.673	0.963	0.621	0.994	0.602	0.985							
Mg	0.489	0.010	0.463	0.030	0.416	0.034	0.388	0.017	0.413	0.045	0.456	0.008	0.480	0.034							
Mn	0.016	0.000	0.016	0.006	0.024	0.003	0.023	0.003	0.022	0.004	0.018	0.005	0.019	0.004							
Total	3.00	3.00	3.00	3.00	3.00	3.00	3.00	3.00	3.00	3.00	3.00	3.00	3.00	3.00							
Cr/(Cr + Al)	0.84	0.97	0.86	0.69	0.86	0.51	0.84	0.66	0.88	0.52	0.84	0.93	0.87	0.81							
Fe ²⁺ /(Fe ²⁺ + Mg)	0.55	0.99	0.57	0.97	0.61	0.97	0.64	0.98	0.62	0.96	0.58	0.99	0.56	0.97							
Mg/(Mg + Fe ²⁺)	0.45	0.01	0.43	0.03	0.39	0.03	0.36	0.02	0.38	0.04	0.42	0.01	0.44	0.03							
Fe ³⁺ /(Fe ³⁺ + Al + Cr)	0.10	0.97	0.10	0.98	0.13	0.98	0.12	0.99	0.14	0.98	0.12	0.98	0.12	0.98							

Oxide (wt. %)	WFD165-SP8			WFD165-SP9			WFD165-SP10			WFD165-SP11			WFD165-SP12			WFD165-SP13			WFD165-SP14		
	Core	Intermediate	Rim	Core	Intermediate	Rim	Core	Intermediate	Rim	Core	Intermediate	Rim	Core	Intermediate	Rim	Core	Intermediate	Rim	Core	Intermediate	Rim
TiO ₂	4.36	7.06	1.45	4.18	10.34	0.46	4.55	6.39	1.47	4.29	1.97	4.18	5.22	0.92	4.51	7.66	4.21	4.14	8.85	4.63	
Al ₂ O ₃	5.78	7.53	0.24	6.06	7.17	0.01	4.76	5.19	0.41	5.34	0.26	5.19	4.54	0.13	5.45	7.87	1.54	5.99	8.49	0.15	
Cr ₂ O ₃	53.18	32.16	0.41	52.91	16.36	0.16	52.50	40.44	0.98	49.99	0.18	53.37	45.98	2.72	52.65	27.81	0.34	52.90	21.04	0.45	
Fe ₂ O ₃	7.23	14.45	64.27	8.80	23.06	66.95	8.53	11.52	63.72	9.38	63.48	8.97	10.15	63.50	8.56	17.63	56.93	7.93	20.17	57.84	
FeO	17.32	35.80	31.78	15.75	39.77	30.89	19.05	31.52	31.94	20.71	32.27	16.56	29.11	30.29	16.61	36.19	34.14	16.42	38.33	34.20	
MgO	12.66	1.09	0.03	13.85	0.37	0.05	11.55	3.29	0.06	9.87	0.05	13.22	4.63	0.68	13.34	1.28	0.15	13.21	0.30	0.16	
MnO	0.40	1.95	0.06	0.31	1.31	0.06	0.54	2.04	0.02	1.02	0.01	0.31	1.49	0.11	0.29	1.90	0.01	0.26	2.04	0.17	
Total	100.92	100.05	98.24	101.87	98.38	98.58	101.48	100.37	98.59	100.60	98.22	101.80	101.12	98.35	101.40	100.34	97.32	100.86	99.22	97.59	
Ti	0.108	0.190	0.043	0.102	0.286	0.014	0.113	0.170	0.043	0.109	0.058	0.102	0.137	0.027	0.111	0.206	0.123	0.102	0.241	0.136	
Al	0.224	0.318	0.011	0.231	0.311	0.001	0.186	0.217	0.019	0.212	0.012	0.200	0.187	0.006	0.210	0.331	0.071	0.231	0.363	0.007	
Cr	1.382	0.911	0.013	1.352	0.476	0.005	1.375	1.135	0.030	1.332	0.006	1.375	1.272	0.084	1.359	0.785	0.010	1.370	0.603	0.014	
Fe ³⁺	0.179	0.390	1.891	0.214	0.639	1.967	0.213	0.307	1.865	0.238	1.867	0.220	0.267	1.857	0.210	0.473	1.672	0.195	0.551	1.707	
Fe ²⁺	0.476	1.073	1.039	0.426	1.225	1.009	0.528	0.935	1.039	0.584	1.055	0.451	0.852	0.984	0.453	1.080	1.114	0.450	1.163	1.121	
Mg	0.621	0.058	0.002	0.667	0.020	0.003	0.571	0.174	0.003	0.496	0.003	0.643	0.241	0.039	0.649	0.068	0.009	0.645	0.016	0.009	
Mn	0.011	0.059	0.002	0.008	0.041	0.002	0.015	0.061	0.001	0.029	0.000	0.008	0.044	0.004	0.008	0.058	0.000	0.007	0.063	0.006	
Total	3.00	3.00	3.00	3.00	3.00	3.00	3.00	3.00	3.00	3.00	3.00	3.00	3.00	3.00	3.00	3.00	3.00	3.00	3.00	3.00	
Cr/(Cr + Al)	0.86	0.74	0.54	0.85	0.60	0.90	0.88	0.84	0.62	0.86	0.32	0.87	0.87	0.93	0.87	0.70	0.13	0.86	0.62	0.67	
Fe ²⁺ /(Fe ²⁺ + Mg)	0.43	0.95	1.00	0.39	0.98	1.00	0.48	0.84	1.00	0.54	1.00	0.41	0.78	0.96	0.41	0.94	0.99	0.41	0.99	0.99	
Mg/(Mg + Fe ²⁺)	0.57	0.05	0.00	0.61	0.02	0.00	0.52	0.16	0.00	0.46	0.00	0.59	0.22	0.04	0.59	0.06	0.01	0.59	0.01	0.01	
Fe ³⁺ /(Fe ³⁺ + Al + Cr)	0.10	0.24	0.99	0.12	0.45	1.00	0.12	0.19	0.97	0.13	0.99	0.12	0.15	0.95	0.12	0.30	0.95	0.11	0.36	0.99	

The trace element concentrations in the xenocrystic spinels from the No.30 kimberlite are shown in Figure 4 and Table 2, with Zn (320–1047 ppm), Ga (6.4–102 ppm), Zr (0.1–11.3 ppm), Nb (0.1–7.1 ppm), and Ni (668–2306 ppm). Most element concentrations are too low to meet the detection limit, and thus, are not shown here.

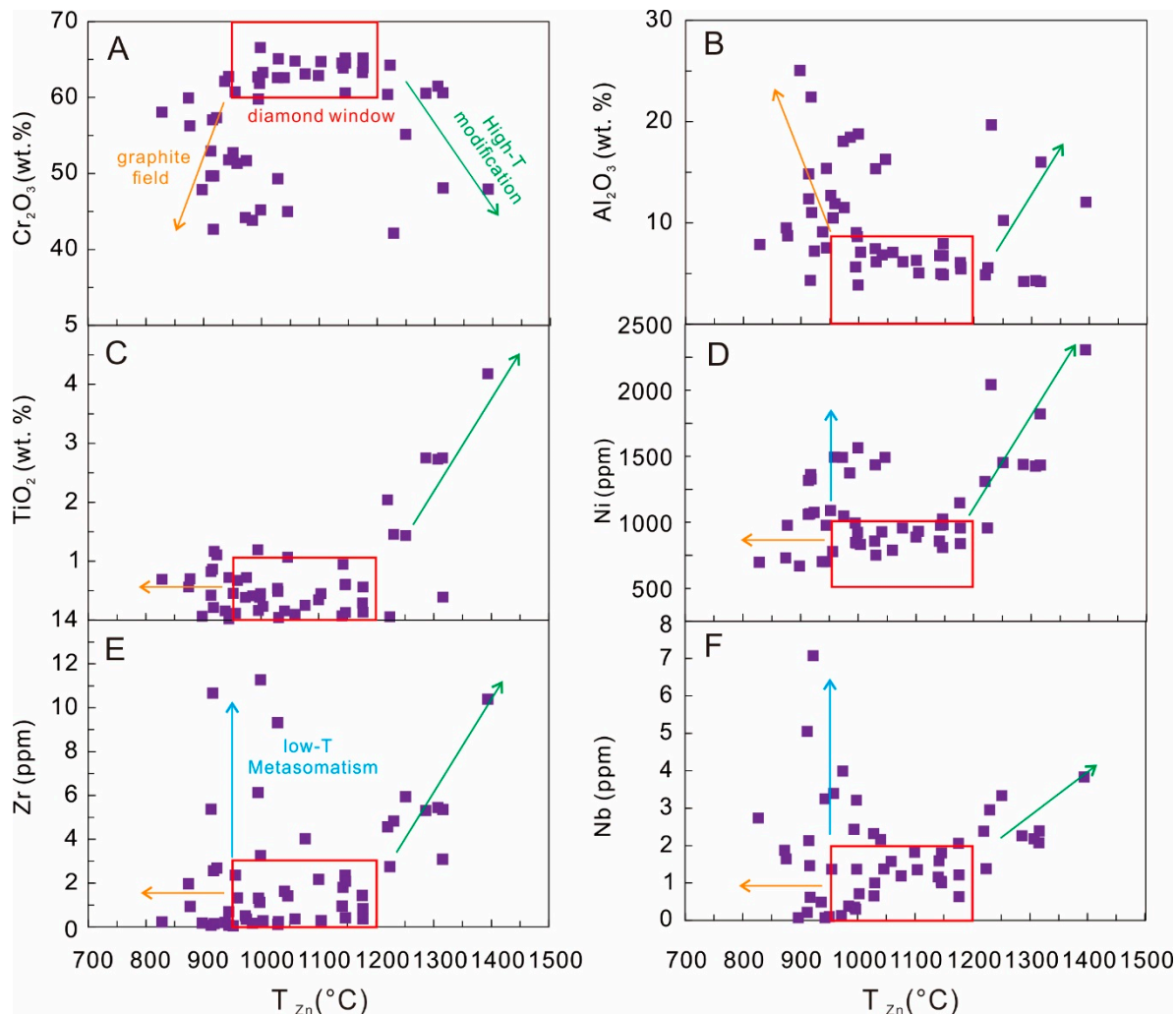


Figure 4. Variations of Cr_2O_3 (A), Al_2O_3 (B), TiO_2 (C), Ni (D), Zr (E), and Nb (F) versus T_{Zn} in the cores of the xenocrystic spinels from the No.30 kimberlite. The T_{Zn} are the temperature estimates based on the Zn-in-chromite thermometer [15].

Table 2. Trace element concentrations and equilibrium temperature estimated using the Zn-in-chromite method [15] in the xenocrystic spinels from the No.30 kimberlite.

ppm	L30-01	L30-02	L30-03	L30-04	L30-05	L30-06	L30-07	L30-08	L30-09	L30-10	L30-11	L30-12	L30-13	L30-14	L30-15	L30-16	L30-17
Zn	1047	452	662	453	571	657	910	850	803	482	698	677	609	358	375	363	359
Ga	85.6	22.7	20.1	40.9	17.3	12.1	52.5	25.9	75.1	27.9	37.8	46.5	24.5	27.4	26.5	27.0	39.2
Zr	0.23	0.83	6.13	1.44	0.36	1.12	1.97	0.17	0.15	1.80	0.51	0.16	0.24	5.35	5.31	5.44	3.09
Nb	2.74	1.22	2.43	2.06	1.57	0.30	1.87	0.07	0.62	1.59	0.12	0.38	1.00	2.39	2.26	2.18	2.07
Ni	696	957	994	1147	788	843	731	668	1327	977	1490	1373	750	1432	1437	1425	1821
T _{Zn} (°C)	828	1177	995	1176	1059	998	874	898	919	1143	973	986	1031	1316	1286	1307	1316
ppm	L30-18	L30-19	L30-20	L30-21	L30-22	L30-23	L30-24	L30-25	L30-26	L30-27	L30-28	L30-29	L30-30	L30-31	L30-32	L30-33	L30-34
Zn	551	610	751	764	723	648	595	729	611	588	478	416	479	655	806	411	320
Ga	15.4	41.5	62.7	29.1	101.5	61.0	38.1	13.8	10.1	51.4	17.2	20.8	26.3	35.5	38.3	65.9	88.0
Zr	4.02	0.11	0.07	0.20	1.32	0.28	1.62	2.36	9.31	1.41	0.41	2.74	2.35	3.25	2.55	4.82	10.39
Nb	1.19	0.65	0.07	0.49	3.39	0.71	2.16	1.37	2.32	1.38	1.00	1.38	1.04	1.37	1.46	2.95	3.83
Ni	957	1435	978	702	1494	832	927	778	858	1491	808	955	1024	1563	1361	2041	2306
T _{Zn} (°C)	1077	1030	944	938	959	1004	1041	956	1029	1047	1147	1224	1146	1000	918	1231	1394
ppm	L30-35	L30-36	L30-37	L30-38	L30-39	L30-40	L30-41	L30-42	L30-43	L30-44	L30-45	L30-46	L30-47	L30-48	L30-49	L30-50	L30-51
Zn	660	655	815	695	478	815	520	419	903	452	751	397	484	736	809	793	524
Ga	6.4	7.4	53.3	79.0	29.0	46.0	29.7	15.1	49.6	13.1	18.6	85.5	17.0	87.8	23.3	39.3	29.6
Zr	1.30	11.3	5.37	0.35	2.08	0.08	0.28	4.56	0.94	0.36	0.70	5.93	0.95	0.05	10.66	2.68	2.16
Nb	0.35	3.21	5.05	3.99	1.80	0.21	1.36	2.38	1.64	0.63	3.25	3.33	1.15	0.10	2.13	7.07	1.82
Ni	846	922	1059	1048	981	1317	931	1308	976	838	701	1451	858	1089	1064	1075	888
T _{Zn} (°C)	996	999	913	975	1147	914	1105	1220	877	1177	944	1251	1141	952	916	924	1100

4. Discussion

4.1. Early Crystallization Sequence

An understanding of the texture and chemical composition of kimberlite minerals is difficult because of the lack of detailed experimental work on the crystallization history of kimberlite magma [22,31]. Commonly, the first minerals to crystallize from the kimberlite magma are olivine phenocrysts and chromite [22]. Within the No.30 kimberlite pipe, chromite in the magmatic spinel was found in the cores of zoned magmatic spinels. The zoning trend in magmatic spinels from the chromite core to the magnetite rim is typical for the kimberlite and magnetite rim and is considered to be a product of late-stage crystallization [22,23]. In addition, an atoll-texture shown in zoned spinel (Figure 1B) is typical in Group I kimberlite [22].

The spinel prism-diagram showing the variation in the composition of spinel is widely used to infer crystallization processes in kimberlite [22,23,32,33]. It uses either ferric iron (oxidized prism) or titanium (reduced prism) as the vertical axis. There are two typical compositional trends in kimberlite: trend 1 from chromite to magnesio-ulvospinel-magnetite and trend 2 of increasing titanium and ferric iron as a function of increasing $Fe^{2+}/(Fe^{2+} + Mg)$ (Figure 3, [23]). Trend 1 is influenced by the high carbonate content of kimberlite melt which causes rapid crystallization of the minerals [23], and trend 2 is generally known to form by the co-crystallization of phlogopite that depletes melt in Mg and Al [22]. As shown in Figure 3, with the increasing of $Fe^{2+}/(Fe^{2+} + Mg)$, $Cr/(Cr + Al)$ decreases and $Fe^{3+}/(Fe^{3+} + Al + Cr)$ increases from the cores to the rims in the magmatic spinels. This compositional trend in Figure 3 is similar to trend 2 but slightly deviates to the right of the outline suggested by Mitchell [22]. This indicates that besides the co-crystallization of phlogopite and spinel, another Mg-rich mineral, such as olivine, must be involved. This is consistent with the proposal by Roeder and Schulze [23] and Bussweiler et al. [34] where trend 2 was shown to be caused by co-crystallization of olivine and phlogopite in kimberlites. In the Al-Cr-Fe³⁺ diagram (Figure 3C), the intermediate zones in the magmatic spinel show the compositional variation to trend 1 but appears different in the other plots (Figure 3A,B). Here, we explained that because the crystallization of large phlogopite prevented new phlogopite nucleation in the vicinity, local Al contents in the kimberlite magma increase during the crystallization of minerals (Table 1), and thus data points in Figure 3C are shifted from Trend 2 to the Trend 1 [23]. In summary, we conclude that spinel, olivine, and phlogopite are crystallized contemporaneously at the beginning of kimberlite crystallization.

4.2. Temperature and Oxygen Fugacity

Co-crystallized spinel-olivine pairs can be used to estimate the temperature and oxygen fugacity (fO_2) of the magma at the time of crystallization. The oxygen fugacity of kimberlite is an important parameter that influences diamond resorption [17,35,36]. Magmatic chromite compositions in this study suggest crystallization together with olivine phenocrysts (see Section 4.1). However, virtually all the olivine phenocrysts in the No.30 kimberlite were altered, and thus, their composition could not be obtained. An alternative method is to use the composition of olivine inclusion within chromite [37] which shows an average $Mg^{\#}$ ($=Mg/(Mg + Fe) \times 100$) of 90. In this study, equilibrium temperatures are estimated using the spinel-olivine Fe/Mg exchange thermometer of O'Neill and Wall [38], as simplified by Ballhaus et al. [25]. As shown in Table 3, the calculated temperatures range from 994 to 1274 °C assuming a pressure of 1 GPa. Pressure has a fairly small effect on temperature (1.5% decrease in temperature from 10 kbar to 1 bar). The oxygen barometer is based on the olivine-orthopyroxene-spinel equilibrium developed by Ballhaus et al. [25]. This barometer requires the presence of orthopyroxene, and for orthopyroxene-undersaturated rocks, the barometer gives maximum oxygen fugacity values [25]. Because the silica activity (a_{SiO_2}) of kimberlites is well below that required to stabilize orthopyroxene [39–43], a correction has to be made to the calculated fO_2 values. Silica activity in the kimberlite can be limited by the groundmass mineral assemblages at a given temperature (T) and pressure (P) [22,30]. In this study, the upper limit of silica activity is

constrained by the presence of monticellite, which is below the diopside-monticellite (Di-Mont) buffer. Silica activity for the Di-Mont buffer was calculated using the thermodynamic data of Holland and Powell [44], and the method of fO_2 adjustment in this study was described in detail by Fedortchouk and Canil [35]. As shown in Table 3, the adjusted fO_2 of the No.30 kimberlite ranges from 1.6 to 2.4 log units below the nickel-nickel oxide (NNO) buffer.

Table 3. Equilibrium temperatures and oxygen fugacities estimated for the No.30 kimberlite magma by Ol-Sp thermobarometry assuming a pressure of 1 GPa.

Sample	Ol-Sp T (°C) ^a	Ol-Sp Oxygen Fugacity ^b			log a_{SiO_2} ^c		Corrected ^d	
		$\Delta \log fO_2^{FMQ}$	$\log fO_2$	$\Delta \log fO_2^{NNO}$	Di-Mont	En-Fo	$\Delta \log fO_2^{FMQ}$	$\Delta \log fO_2^{NNO}$
WFD148-SP1	1249	1.5	-9.8	1.0	-1.40	-0.41	-1.5	-2.0
WFD148-SP2	1218	1.5	-10.1	1.1	-1.46	-0.43	-1.6	-2.0
WFD148-SP3	1168	1.9	-10.5	1.5	-1.54	-0.46	-1.4	-1.8
WFD148-SP4	1102	1.7	-11.7	1.3	-1.65	-0.50	-1.7	-2.1
WFD148-SP5	1181	2.0	-10.1	1.6	-1.52	-0.45	-1.1	-1.6
WFD148-SP6	1214	1.8	-10.0	1.4	-1.46	-0.43	-1.3	-1.7
WFD148-SP7	1265	1.6	-9.4	1.2	-1.38	-0.40	-1.3	-1.7
WFD165-SP8	1170	1.2	-6.9	0.8	-1.54	-0.46	-2.0	-2.4
WFD165-SP9	1274	1.5	-5.5	1.1	-1.36	-0.40	-1.4	-1.8
WFD165-SP10	1107	1.6	-7.3	1.2	-1.65	-0.50	-1.8	-2.2
WFD165-SP11	994	1.9	-8.6	1.5	-1.84	-0.57	-1.9	-2.4
WFD165-SP12	1233	1.6	-5.9	1.2	-1.43	-0.42	-1.5	-1.9
WFD165-SP13	1240	1.5	-5.9	1.1	-1.42	-0.42	-1.5	-1.9
WFD165-SP14	1217	1.3	-6.3	1.0	-1.46	-0.43	-1.7	-2.1

^a Temperatures calculated from the Fe/Mg exchange Ol-Sp thermometer of O'Neill and Wall [38] and Ballhaus et al. [25];

^b Oxygen fugacities at 1 GPa calculated for the fayalite-magnetite-quartz (FMQ) buffer from the oxygen barometer by Ballhaus et al. [25]; ^c Silica activity of Diopside-Monticellite (Di-Mont) and Enstatite-Forsterite (En-Fo) buffers calculated using thermodynamic data of Holland and Powell [44]. ^d Corrected values of oxygen fugacities of kimberlite calculated for silica activity of Diopside-Monticellite buffer [35]. The equation for nickel-nickel oxide (NNO) buffer is from Ballhaus et al. [25].

4.3. Trace Element Concentration in the Diamond Window

In diamond exploration, it is important to discriminate the indicator mineral that is derived from diamond stability field and that from the diamond-barren or no-diamond field. The composition characteristics of minerals in the diamond stability field are based on mineral inclusions in the diamond [14]. However, the relative scarcity of mineral inclusions in the diamond limits a comprehensive understanding of these characteristics. Griffin and Ryan [4] describe the diamond stability field as the “diamond window”, which can be defined as the range of T_{Ni} (Ni-in-garnet thermometer) between the intersection of geotherm with the diamond-graphite equilibrium curve and the base of the lithosphere (unmodified lithosphere). According to the estimate by Griffin and Ryan's for the Liaoning Province, there is a diamond window with temperatures between 900–1250 °C [4]. In this study, we use the major and trace element composition in xenocrystic spinels to redefine a slightly narrower temperature range (950–1200 °C) for the diamond window. In contrast to the approach by Griffin and Ryan, we use a multi-element approach to constrain the temperature range.

As shown in Figure 4, the distribution of major and trace element concentrations show an abrupt change when T_{Zn} (Zn-in-chromite temperature, [15]) moves through 950 and 1200 °C. The compositions in the xenocrystic spinel with temperature 950–1200 °C are nearly constant: Cr_2O_3 (60–66 wt. %), Al_2O_3 (0–8 wt. %), TiO_2 (0–1 wt. %), Ni (500–1000 ppm), Zr (0–3 ppm), and Nb (0–2 ppm), and are consistent with that of chromite inclusions in diamonds [14]. The Ni, Zr, and Nb concentrations in spinels with temperatures between 950–1200 °C are lower than those with temperatures higher than 1200 °C (Figure 4), which may indicate that higher-T spinels have interacted with asthenosphere-derived melts [4,45–47]. For the spinels with temperatures below 950 °C, the spinels show the hybrid features: inner feature of spinels in the graphite field (low Cr_2O_3 and high Al_2O_3 contents) and low-T modification (increasing Zr and Nb concentrations). Due to the paucity of studies on chromite metasomatism, it is difficult to distinguish between metasomatism and original trace element signatures. Because some low-T metasomatism, especially carbonatite or

COH metasomatism can be related to diamond formation [11–13,48–50], the lower T boundary of the diamond window is unclear, and further studies are needed to constrain this more precisely.

4.4. Diamond Potential in Kimberlite

Diamond formation in the mantle is generally considered to be a metasomatic process [51,52]. The metasomatic agents react with the mantle rocks in which they infiltrate, and the diamond crystallizes as a consequence of different redox reactions. The oxidation state is likely controlled by $\text{Fe}^0\text{-Fe}^{2+}\text{-Fe}^{3+}$ components in oxide minerals like chromite [12]. Malkovets et al. [16] suggested that garnet and chromite play an important role in the diamond formation. Therefore, garnet and chromite are important indicators of minerals. In general, diamondiferous kimberlites sample both garnet and chromite, but low-grade pipes tend to sample only chromite [16]. As discussed in Section 4.3, the diamond window beneath the Liaoning Province is redefined. If kimberlite captures garnet and chromite from this field at the same time, it has great potential to capture diamonds without considering other factors.

The equilibrium temperatures in the garnet xenocrysts from the No.30 kimberlite pipe calculated using single grain Ni-in-garnet thermometer [53] ranges from 1100 to 1350 °C, with a peak at about 1150 °C (Figure 5; [27]). However, the calculated equilibrium temperatures of xenocrystic chromites from the No.30 kimberlite using single grain Zn-in-chromite [15] vary from 828 to 1394 °C, with a peak at about 950 °C (Figure 5, Table 2). The temperature distribution curves show that garnets and chromites are not distributed in the same way, which is similar to the low-grade Zarnitsa and Solokha kimberlites, and different from the high-grade Udachnaya and Lomonosova kimberlites [16]. It indicates that garnets have not overgrown with chromites and diamonds haven't widely formed in mantle rock samples by the kimberlite (Figure 5) [16]. Thus even though the No.30 kimberlite sampled the garnet/chromite-bearing mantle rock from the diamond stability field, the diamond grade in the kimberlite is low because the sampled mantle rocks are diamond-barren [16] and the diamond window is narrow.

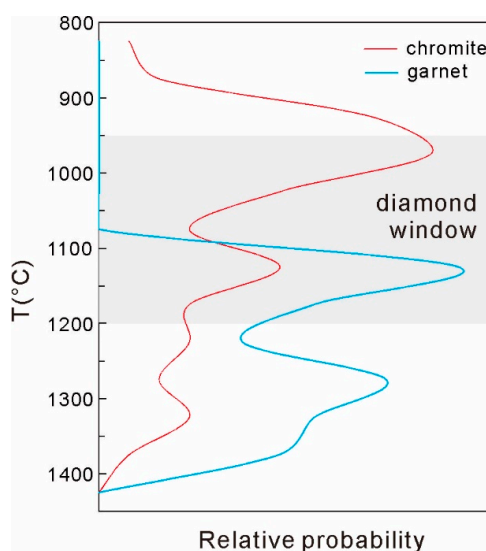


Figure 5. Temperature (depth) distribution of xenocrystic garnets and chromites from the No.30 kimberlite. Equilibrium temperatures of garnets [27] are calculated using the Ni-in-garnet thermometer [53], and equilibrium temperatures with the cores of xenocrystic spinels are estimated using Zn-in-chromite thermometer [15].

As previously suggested by Zhu et al. [26], the oxidizing environment also contributes to low-grade diamonds in the No.30 kimberlite. The estimated $f\text{O}_2$ of the No.30 kimberlite magma is 1.6–2.4 log units relative to NNO buffer during the early magmatism (Table 3). Ideally, the $f\text{O}_2$ in the No.30 kimberlite is compared with that of other kimberlites with different diamond grades in the North China Craton.

However, there is no such study on fO_2 or related studies. So in this study, we compare fO_2 of the No.30 kimberlite magma with fO_2 estimates for the Lac de Gras kimberlites (Slave craton, Canada) with different diamond grades [17]. As shown in Figure 6, the comparison shows that the fO_2 of the No.30 kimberlite magma is most similar to the fO_2 of the low-grade Ranch Lake kimberlite and significantly higher than the fO_2 of high-grade Misery and Beartooth kimberlites in the Lac de Gras area. As suggested by many researchers, high fO_2 promotes diamond resorption [17,20,21]. We conclude that diamond resorption in the No.30 kimberlite was strong, which contributed to the generally low diamond grade.

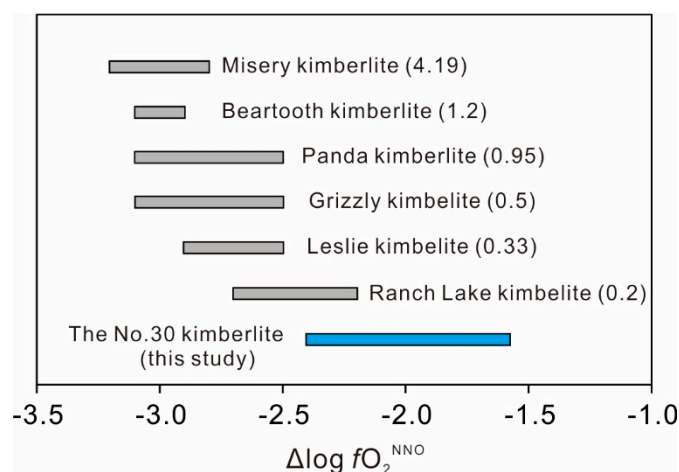


Figure 6. Estimated $\log fO_2$ oxygen fugacity conditions (ΔNNO ; derived from Ol-Sp thermobarometry at an assumed pressure of 1 GPa) for the No.30 kimberlite (this study) compared with Misery, Beartooth, Panda, Grizzly, Leslie, and Ranch Lake kimberlites from the Lac de Gras area [17] (the numbers in parentheses represent diamond grades of kimberlites in units of carats/ton).

5. Conclusions

Magmatic spinels in the No.30 kimberlite pipe are euhedral to subhedral, 20–60 μm in diameter. These spinels are zoned from Ti-Al-Mg chromite through Ti-Al chromite to magnetite, suggesting co-crystallization of spinel and olivine phenocrysts during early kimberlite crystallization.

At an assumed pressure of 1 GPa, temperatures and oxygen fugacity of kimberlite magma are estimated in a range of 994–1274 $^{\circ}\text{C}$ and 1.6–2.4 log units below the NNO buffer, respectively, suggesting strong diamond resorption during kimberlite magmatism.

Temperature distribution curves of xenocrystic garnet and chromite show that the sampling of garnet does not overlap with that of chromite, which suggests the mantle rock sampled by the kimberlite is diamond-barren.

Low-diamond capture and heavy-diamond resorption during kimberlite magmatism lead to low-diamond grade in the No.30 kimberlite.

Supplementary Materials: The following are available online at <http://www.mdpi.com/2075-163X/9/6/382/s1>, Table S1: Trace elements chemistry for standard.

Author Contributions: R.-Z.Z., P.N., G.-G.W., and J.-Y.D. did the field work; R.-Z.Z. analyzed the samples and interpreted the results; R.-Z.Z. and P.N. wrote the paper; R.-Z.Z., P.N., G.-G.W. and J.-Y.D. revised the manuscript. All authors read and approved the manuscript.

Funding: This research was funded by the Ministry of Land and Resources of the PRC (Grant No. 201404025) and China Scholarship Council (No. 201706190172).

Acknowledgments: We thank N.K., S.-N.L., T.B., A.-D.Z., B.H., and L.-L.C. for their help during field work. We would like to thank W.-L.Z. for their technical guide during the analysis of the major elements of spinel. We appreciate L.L. and J.-F.G. for their help during the analysis of the trace elements of the spinel. Thanks to the State Key Laboratory for Mineral Deposit Research, Nanjing University for their assistance in the experiment. We appreciate the constructive comments from the Academic Editor and two anonymous reviewers.

Conflicts of Interest: The authors declare no conflict of interest.

References

1. Hardman, M.F.; Pearson, D.G.; Stachel, T.; Sweeney, R.J. Statistical approaches to the discrimination of crust-and mantle-derived low-Cr garnet–Major-element-based methods and their application in diamond exploration. *J. Geochem. Explor.* **2018**, *186*, 24–35. [[CrossRef](#)]
2. Grütter, H.S.; Gurney, J.J.; Menzies, A.H.; Winter, F. An updated classification scheme for mantle-derived garnet, for use by diamond explorers. *Lithos* **2004**, *77*, 841–857. [[CrossRef](#)]
3. Schulze, D.J. A classification scheme for mantle-derived garnets in kimberlite: A tool for investigating the mantle and exploring for diamonds. *Lithos* **2003**, *71*, 195–213. [[CrossRef](#)]
4. Griffin, W.; Ryan, C. Trace elements in indicator minerals: Area selection and target evaluation in diamond exploration. *J. Geochem. Explor.* **1995**, *53*, 311–337. [[CrossRef](#)]
5. Griffin, W.; Sobolev, N.; Ryan, C.; Pokhilenko, N.; Win, T.; Yefimova, E. Trace elements in garnets and chromites: Diamond formation in the Siberian lithosphere. *Lithos* **1993**, *29*, 235–256. [[CrossRef](#)]
6. Gurney, J.J. A correlation between garnets and diamonds in kimberlites. In *Kimberlite Occurrence and Origin: A Basis for Conceptual Models in Exploration*; University of Western Australia: South Perth, Australia, 1984; Volume 8, pp. 143–166.
7. Sobolev, N.V.; Lavrent'ev, Y.G.; Pokhilenko, N.P.; Usova, L.V. Chrome-rich garnets from the kimberlites of Yakutia and their parageneses. *Contr. Mineral. Petrol.* **1973**, *40*, 39–52. [[CrossRef](#)]
8. Carmody, L.; Taylor, L.A.; Thaisen, K.G.; Tychkov, N.; Bodnar, R.J.; Sobolev, N.V.; Pokhilenko, L.N.; Pokhilenko, N.P. Ilmenite as a diamond indicator mineral in the Siberian craton: A tool to predict diamond potential. *Econ. Geol.* **2014**, *109*, 775–783. [[CrossRef](#)]
9. Wyatt, B.A.; Baumgartner, M.; Anckar, E.; Grutter, H. Compositional classification of “kimberlitic” and “non-kimberlitic” ilmenite. *Lithos* **2004**, *77*, 819–840. [[CrossRef](#)]
10. Schulze, D.J. Origins of chromian and aluminous spinel macrocrysts from kimberlites in southern Africa. *Can. Mineral.* **2001**, *39*, 361–376. [[CrossRef](#)]
11. Gurney, J.J.; Helmstaedt, H.H.; Richardson, S.H.; Shirey, S.B. Diamonds through Time. *Econ. Geol.* **2010**, *105*, 689–712. [[CrossRef](#)]
12. Shirey, S.B.; Cartigny, P.; Frost, D.J.; Keshav, S.; Nestola, F.; Nimis, P.; Pearson, D.G.; Sobolev, N.V.; Walter, M.J. Diamonds and the geology of Mantle carbon. In *Carbon in Earth*; Hazen, R.M., Jones, A.P., Baross, J.A., Eds.; Mineralogical Society of America: Chantilly, VA, USA, 2013; Volume 75, pp. 355–421.
13. Gurney, J.J.; Helmstaedt, H.H.; Le Roex, A.P.; Nowicki, T.E.; Richardson, S.H.; Westerlund, K.J. Diamonds: Crustal distribution and formation processes in time and space and an integrated deposit model. *Econ. Geol.* **2005**, *100*, 143–177.
14. Gurney, J.J.P.; Zweistra, P. The interpretation of the major element compositions of mantle minerals in diamond exploration. *J. Geochem. Explor.* **1995**, *53*, 293–309. [[CrossRef](#)]
15. Ryan, C.G.; Griffin, W.L.; Pearson, N.J. Garnet geotherms: Pressure-temperature data from Cr-pyropite garnet xenocrysts in volcanic rocks. *J. Geophys. Res. Solid Earth* **1996**, *101*, 5611–5625. [[CrossRef](#)]
16. Malkovets, V.G.; Griffin, W.L.; O'Reilly, S.Y.; Wood, B.J. Diamond, subcalcic garnet, and mantle metasomatism: Kimberlite sampling patterns define the link. *Geology* **2007**, *35*, 339–342. [[CrossRef](#)]
17. Fedortchouk, Y.; Canil, D.; Carlson, J.A. Dissolution forms in Lac de Gras diamonds and their relationship to the temperature and redox state of kimberlite magma. *Contr. Mineral. Petrol.* **2005**, *150*, 54–69. [[CrossRef](#)]
18. Gurney, J.J.; Hildebrand, P.R.; Carlson, J.A.; Fedortchouk, Y.; Dyck, D.R. The morphological characteristics of diamonds from the Ekati property, Northwest Territories, Canada. *Lithos* **2004**, *77*, 21–38. [[CrossRef](#)]
19. Alam, M.; Sun, Q. The kinetics of chemical vapor deposited diamond-oxygen reaction. *J. Mater. Res.* **1993**, *8*, 2870–2878. [[CrossRef](#)]
20. Sonin, V.; Pokhilenko, L.; Pokhilenko, N.; Fedorov, I. Diamond oxidation rate as related to oxygen fugacity. *Geol. Ore Depos.* **2000**, *42*, 496–502.
21. Kozai, Y.; Arima, M. Diamond dissolution in kimberlite and lamproite melts at deep crustal conditions. In Proceedings of the 8th International Kimberlite Conference, Victoria, BC, Canada, 22–27 June 2003; Extended Abstracts.
22. Mitchell, R.H. *Kimberlites*; Plenum: New York, NY, USA, 1986.

23. Roeder, P.L.; Schulze, D.J. Crystallization of groundmass spinel in kimberlite. *J. Petrol.* **2008**, *49*, 1473–1495. [[CrossRef](#)]
24. Van Straaten, B.I.; Kopylova, M.G.; Russell, J.; Webb, K.J.; Smith, B.H.S. Discrimination of diamond resource and non-resource domains in the Victor North pyroclastic kimberlite, Canada. *J. Volcanol. Geotherm. Res.* **2008**, *174*, 128–138. [[CrossRef](#)]
25. Ballhaus, C.; Berry, R.F.; Green, D.H. High pressure experimental calibration of the olivine-orthopyroxene-spinel oxygen geobarometer: Implications for the oxidation state of the upper mantle. *Contr. Mineral. Petrol.* **1991**, *107*, 27–40. [[CrossRef](#)]
26. Zhu, R.Z.; Ni, P.; Ding, J.Y.; Wang, D.Z.; Ju, Y.; Kang, N.; Wang, G.G. Petrography, chemical composition, and Raman spectra of chrome spinel: Constraints on the diamond potential of the No. 30 pipe kimberlite in Wafangdian, North China Craton. *Ore Geol. Rev.* **2017**, *91*, 896–905. [[CrossRef](#)]
27. Zhu, R.Z.; Ni, P.; Ding, J.Y.; Wang, G.G.; Fan, M.S.; Li, S.N. Metasomatic processes in the lithosphere mantle beneath the No.30 kimberlite (Wafangdian region, North China Craton). *Can. Mineral.* **2019**, *57*, 1–19. [[CrossRef](#)]
28. Droop, G. A general equation for estimating Fe³⁺ concentrations in ferromagnesian silicates and oxides from microprobe analyses, using stoichiometric criteria. *Mineral. Mag.* **1987**, *51*, 431–435. [[CrossRef](#)]
29. Liu, Y.S.; Hu, Z.C.; Gao, S.; Günther, D.; Xu, J.; Gao, C.G.; Chen, H.H. In situ analysis of major and trace elements of anhydrous minerals by LA-ICP-MS without applying an internal standard. *Chem. Geol.* **2008**, *257*, 34–43. [[CrossRef](#)]
30. Mitchell, R.H. *Kimberlites, Orangeites, Lamproites, Melilitites, and Minettes: A Petrographic Atlas*; Almaz Press: Thunder Bay, ON, Canada, 1997; p. 243.
31. Mitchell, R.H. Kimberlites and orangeites. In *Kimberlites, Orangeites, and Related Rocks*; Plenum Press: New York, NY, USA, 1995.
32. Haggerty, S.E. The chemistry and genesis of opaque minerals in kimberlites. *Phys. Chem. Earth* **1975**, *9*, 295–307. [[CrossRef](#)]
33. Irvine, T. Chromian spinel as a petrogenetic indicator: Part 1. Theory. *Can. J. Earth Sci.* **1965**, *2*, 648–672. [[CrossRef](#)]
34. Bussweiler, Y.; Stone, R.S.; Pearson, D.G.; Luth, R.W.; Stachel, T.; Kjarsgaard, B.A.; Menzies, A. The evolution of calcite-bearing kimberlites by melt-rock reaction: Evidence from polymineralic inclusions within clinopyroxene and garnet megacrysts from Lac de Gras kimberlites, Canada. *Contr. Mineral. Petrol.* **2016**, *171*, 65. [[CrossRef](#)]
35. Fedortchouk, Y.; Canil, D. Intensive variables in kimberlite magmas, Lac de Gras, Canada and implications for diamond survival. *J. Petrol.* **2004**, *45*, 1725–1745. [[CrossRef](#)]
36. Kozai, Y.; Arima, M. Experimental study on diamond dissolution in kimberlitic and lamproitic melts at 1300–1420 °C and 1 GPa with controlled oxygen partial pressure. *Am. Miner.* **2005**, *90*, 1759–1766. [[CrossRef](#)]
37. Zhao, D.; Zhang, Y.; Essene, E.J. Electron probe microanalysis and microscopy: Principles and applications in characterization of mineral inclusions in chromite from diamond deposit. *Ore Geol. Rev.* **2015**, *65*, 733–748. [[CrossRef](#)]
38. O'Neill, H.S.C.; Wall, V. The Olivine-Orthopyroxene-Spinel oxygen geobarometer, the nickel precipitation curve, and the oxygen fugacity of the Earth's Upper Mantle. *J. Petrol.* **1987**, *28*, 1169–1191. [[CrossRef](#)]
39. Sharygin, I.S.; Litasov, K.D.; Shatskiy, A.; Safonov, O.G.; Golovin, A.V.; Ohtani, E.; Pokhilenko, N.P. Experimental constraints on orthopyroxene dissolution in alkali-carbonate melts in the lithospheric mantle: Implications for kimberlite melt composition and magma ascent. *Chem. Geol.* **2017**, *455*, 44–56. [[CrossRef](#)]
40. Kamenetsky, V.S.; Yaxley, G.M. Carbonate–silicate liquid immiscibility in the mantle propels kimberlite magma ascent. *Geochim. Cosmochim. Acta* **2015**, *158*, 48–56. [[CrossRef](#)]
41. Kamenetsky, V.S.; Kamenetsky, M.B.; Sobolev, A.V.; Golovin, A.V.; Sharygin, V.V.; Pokhilenko, N.P.; Sobolev, N.V. Can pyroxenes be liquidus minerals in the kimberlite magma? *Lithos* **2009**, *112*, 213–222. [[CrossRef](#)]
42. Brett, R.C.; Russell, J.; Moss, S. Origin of olivine in kimberlite: Phenocryst or impostor? *Lithos* **2009**, *112*, 201–212. [[CrossRef](#)]
43. Barker, D.S. Calculated silica activities in carbonatite liquids. *Contr. Mineral. Petrol.* **2001**, *141*, 704–709. [[CrossRef](#)]
44. Holland, T.; Powell, R. An internally consistent thermodynamic data set for phases of petrological interest. *J. Metamorph. Geol.* **1998**, *16*, 309–343. [[CrossRef](#)]

45. Agashev, A.M.; Ionov, D.A.; Pokhilenko, N.P.; Golovin, A.V.; Cherepanova, Y.; Sharygin, I.S. Metasomatism in lithospheric mantle roots: Constraints from whole-rock and mineral chemical composition of deformed peridotite xenoliths from kimberlite pipe Udachnaya. *Lithos* **2013**, *160–161*, 201–215. [[CrossRef](#)]
46. Sharygin, I.S.; Litasov, K.D.; Shatskiy, A.; Golovin, A.V.; Ohtani, E.; Pokhilenko, N.P. Melting phase relations of the Udachnaya-East Group-I kimberlite at 3.0–6.5 GPa: Experimental evidence for alkali-carbonatite composition of primary kimberlite melts and implications for mantle plumes. *Gondwana Res.* **2015**, *28*, 1391–1414. [[CrossRef](#)]
47. Nixon, P.H. A review of mantle xenoliths and their role in diamond exploration. *J. Geodyn.* **1995**, *20*, 305–329. [[CrossRef](#)]
48. Stachel, T.; Aulbach, S.; Brey, G.P.; Harris, J.W.; Leost, I.; Tappert, R.; Viljoen, K.S. The trace element composition of silicate inclusions in diamonds: A review. *Lithos* **2004**, *77*, 1–19. [[CrossRef](#)]
49. Stachel, T.; Harris, J.W. The origin of cratonic diamonds—Constraints from mineral inclusions. *Ore Geol. Rev.* **2008**, *34*, 5–32. [[CrossRef](#)]
50. Stachel, T.; Harris, J.W. Formation of diamond in the Earth’s mantle. *J. Phys. Condens. Matter* **2009**, *21*, 364206. [[CrossRef](#)]
51. Haggerty, S.E. A diamond trilogy: Superplumes, supercontinents, and supernovae. *Science* **1999**, *285*, 851–860. [[CrossRef](#)]
52. Stachel, T.; Brey, G.P.; Harris, J.W. Inclusions in sublithospheric diamonds: Glimpses of deep Earth. *Elements* **2005**, *1*, 73–78. [[CrossRef](#)]
53. Canil, D. The Ni-in-garnet geothermometer: Calibration at natural abundances. *Contr. Mineral. Petrol.* **1999**, *136*, 240–246. [[CrossRef](#)]



© 2019 by the authors. Licensee MDPI, Basel, Switzerland. This article is an open access article distributed under the terms and conditions of the Creative Commons Attribution (CC BY) license (<http://creativecommons.org/licenses/by/4.0/>).